Nanoscale

PAPER

View Article Online
View Journal | View Issue

Cite this: *Nanoscale*, 2024, **16**, 10779

Mitigating substrate effects of van der Waals semiconductors using perfluoropolyether self-assembled monolayers†

Dae Young Park, ‡[a] Hyeong Chan Suh,‡[a] Seungho Bang,[a] Ju Chan Lee,[b] Jaekak Yoo,[a] Hayoung Ko,[b] Soo Ho Choi,[b] Ki Kang Kim,[b] Seung Mi Lee,[c] Seong Chu Lim,[b] Tschang-Uh Nahm[a] and Mun Seok Jeong *[a]

Received 5th January 2024,
Accepted 26th April 2024

DOI: 10.1039/d4nr00061g

rsc.li/nanoscale

The properties of transition metal dichalcogenides (TMDCs) are critically dependent on the dielectric constant of substrates, which significantly limits their application. To address this issue, we used a perfluorinated polyether (PFPE) self-assembled monolayer (SAM) with low surface energy to increase the van der Waals (vdW) gap between TMDCs and the substrate, thereby reducing the interaction between them. This resulted in a reduction in the subthreshold swing value, an increase in the photoluminescence intensity of excitons, and a decrease in the doping effect by the substrate. This work will provide a new way to control the TMDC/dielectric interface and contribute to expanding the applicability of TMDCs.

1 Introduction

The excellent physical, optical, and electrical properties of two-dimensional (2D) transition metal dichalcogenides (TMDCs) with weak van der Waals (vdW) interaction of layers have triggered intensive studies in the fields of optoelectronics,[1,2] electronics,[3] and catalysts.[4,5] However, their intrinsic properties are crucially affected by the conditions of interfaces, such as air, electrodes, and dielectric substrates due to the atomically low thickness.[6] In particular, the formation of broken interfaces by deposition process, abundance of charge puddles, and roughness of dielectric substrates mainly affect the intrinsic properties of 2D materials.[7–12] Thus, interface engineering at the TMDC/substrate junction is essential to achieve superior optical and electrical properties of 2D TMDCs in both fundamental studies and applications.

To eliminate the effects of the TMDC/substrate interface, various methods such as the suspension of TMDCs and the insertion of a buffer layer including hexagonal boron nitride (hBN), metal oxides, and polymers have been studied.[11–15] Among them, the suspension of TMDCs has been intensively studied, particularly in freestanding structures, as it significantly improves their optical and electrical properties.[11] Furthermore, the suspended MoS_2 field effect transistor (FET) showed the value of subthreshold slopes close to the thermodynamic limit with a high on/off ratio exceeding 10^7.[12] However, large strains at the TMDC/nanostructure interface are inevitable and can even tear TMDCs.

In another approach to eliminate the interface effects, hBN was inserted to block charge puddles on the substrate surface and provide an atomically sharp interface.[15] These advantages due to hBN insertion triggered many studies on TMDCs with hBN and physical properties of TMDCs have been greatly improved.[16,17] In general, hBN has been prepared in numerous studies *via* mechanical exfoliation or chemical vapor deposition (CVD). However, mechanically exfoliated hBN has a small lateral size with poor reproducibility[16,17] and the growth of a sufficient thickness of hBN for wafer scale by a CVD method has been difficult due to the low solubility of the precursor in metal catalysts.[18,19] Despite continuous efforts to eliminate interfacial effects, bottlenecks in interfacial engineering, such as inevitable deformation and the small lateral size of the buffer layer, still remain. In addition, the effect of vdW distance between TMDCs and the substrate has not been understood clearly although the interfacial effect is also crucial with the distance.

In this study, we fabricated a self-assembled monolayer (SAM) of commercial perfluorinated polyether (PFPE) named S10 on a SiO_2/Si substrate, and the monolayer of CVD-grown

[a]*Department of Physics, Hanyang University, Seoul 04763, Republic of Korea. E-mail: mjeong@hanyang.ac.kr*
[b]*Department of Energy Science, Sungkyunkwan University, Suwon 16419, Republic of Korea*
[c]*Korea Research Institute of Standards and Science, Daejeon 34114, Republic of Korea*

†Electronic supplementary information (ESI) available: XPS spectra of S10 and SiO_2 substrate, binding energy of TMDCs on S10 and SiO_2 substrate, the electrical transport of MoS_2 FET depending on substrate, the atomic charge distribution of TMDCs on S10. See DOI: https://doi.org/10.1039/d4nr00061g

‡These authors contributed equally.

TMDCs was transferred to a substrate coated with S10. Through atomic force microscopy (AFM) measurement, the extended vdW gap of TMDCs/S10 more than SiO_2 was observed due to the low surface energy of S10. Because of the expansion of the vdW gap, the PL intensities were enhanced several times without any change in Raman shift related to strain relaxation and doping. This phenomenon was reconfirmed by the fact that the average values of the subthreshold swing in the MoS_2 field effect transistor decreased from 4.75 V dec^{-1} to 2.61 V dec^{-1} even though the defect density of the dielectric interface is increased. This 2D material/dielectric interface engineering using PFPE can help solve interface issues to suppress the unique properties of TMDCs.

2 Experimental

2.1 Materials

Fluorolink S10 (commercial PFPE) and perfluorinated solvent (Novec 7100) were purchased from Solvay and 3M™, respectively. Isopropyl alcohol (IPA, ACS reagent, 99.5%), acetic acid (glacial, ACS reagent, 99.7%), acetone (ACS reagent, 99.5%), and poly(propylene carbonate) (PPC, M_n 50 000) were received from Sigma Aldrich. Polymethyl methacrylate (PMMA A4) was bought from MicroChem. Polydimethylsiloxane (PDMS, Sylgard 184 kit) was received from Dow silicones corporation. All chemicals were used without further purification.

2.2. Growth of monolayer (1L) TMDCs by a CVD method

For the preparation of 1L TMDCs, sodium tungstate/molybdate (Na_2WO_4/Na_2MoO_4, ACS reagent, Sigma Aldrich) and sulfur (S) or selenium (Se) powder (>99.5%, Sigma Aldrich) were used as the precursors of transition metals and chalcogens, respectively. The transition metal precursor was dissolved in deionized (DI) water at a concentration of 0.0125 M. This liquid precursor was then coated onto a SiO_2/Si substrate using a spin-coater at 3000 rpm for 30 seconds. The prepared SiO_2/Si substrate and chalcogen powder were positioned at two different locations within a two-zone CVD system. Each zone was heated to 780 °C and 210 °C over a period of 6 minutes and maintained at these temperatures for 24 minutes, respectively, under atmospheric pressure with N_2 flow at 550 sccm and H_2 flow at 4 sccm. Subsequently, the system was rapidly cooled down to room temperature.

2.3 Preparation and coating of S10 solution

For the coating process, hydrolysis and condensation of PFPE containing a silane group must be performed with an acid catalyst. The procedure was performed according to the instructions provided by Solvay. Briefly, 0.1% of S10, 0.4% of deionized water (DI), 0.1% of acetic acid, and 99.4% of IPA were mixed with weight percent ratio, respectively. To complete the hydrolysis and condensation reaction, the solution was kept under continuous stirring for 24 h. The SiO_2/Si substrate (300 nm SiO_2) was washed with acetone, DI, and IPA under sonication for 10 min, respectively. The spin coating of solution was conducted at 3000 rpm for 30 s and the substrate was annealed at 150 °C for 15 min.

2.4 Device fabrication

A highly p-doped silicon waver with 300 nm thickness of SiO_2 was applied as a dielectric and gate electrode. Silicon wafer was washed with acetone, DI, and IPA under sonication for 10 min, respectively. For the bottom electrode deposition, photo lithography was conducted with AZ-GXR-601 PR (14cp) as the photoresist, which was developed by AZ-300 MIF. Gold and titanium were deposited by a thermal deposition system under a high-vacuum condition. To cover the selective area of S10, photolithography was performed again. Finally, CVD-grown MoS_2 was transferred onto the fabricated bottom electrode using a hand-made dry transfer system with a PPC/PDMS stamp.

2.5 Characterization

The electrical properties were measured using a semiconductor characterization system (Keithley 4200-SCS) under vacuum conditions ($<10^{-3}$ Torr). XPS was performed using a Thermo Scientific Nexsa instrument under high-vacuum conditions ($<10^{-6}$ Torr). A low-power Al K X-ray beam with 10–400 μm spot size was incident on the sample with 30 degrees of incident angle. The Raman and photoluminescence spectra were recorded using a confocal imaging system (LabRam HRevo, HORIBA) with a 532 nm laser. The morphology of TMDCs/S10 was measured using an AFM (XE-100, Park system).

2.6 Theoretical calculations

To determine electron populations of TMDCs on S10, quantum mechanical calculations using the DMOL3 code as implemented in the BIOVIA Materials Studio platform were done and the contributions to the atomic charge from each atomic orbital on each atom were calculated by the Mulliken population analysis method. Detailed process is shown in ESI note 1.†

3 Results and discussion

3.1 Expansion of van der Waals distance

The schematic procedures of the wet transfer of TMDCs onto the S10-coated substrate are shown in Fig. 1a. The detailed process is explained in the experimental part. The photolithography process was performed to fabricate a half-covered SiO_2 substrate using a photoresist to directly compare the S10 effect. A half-covered SiO_2 substrate spin-coated with the S10 solution was annealed in a convection oven. Subsequently, CVD-grown TMDCs were transferred to a half-coated substrate with S10. In Fig. 1b, the vdW gap of MoS_2/S10 is measured as 3.35 nm, which is larger than that of MoS_2/SiO_2 (1.35 nm). In addition, the expanded vdW distance of other TMDCs on S10 around 4 nm is observed, greater than 1 nm on SiO_2, as shown

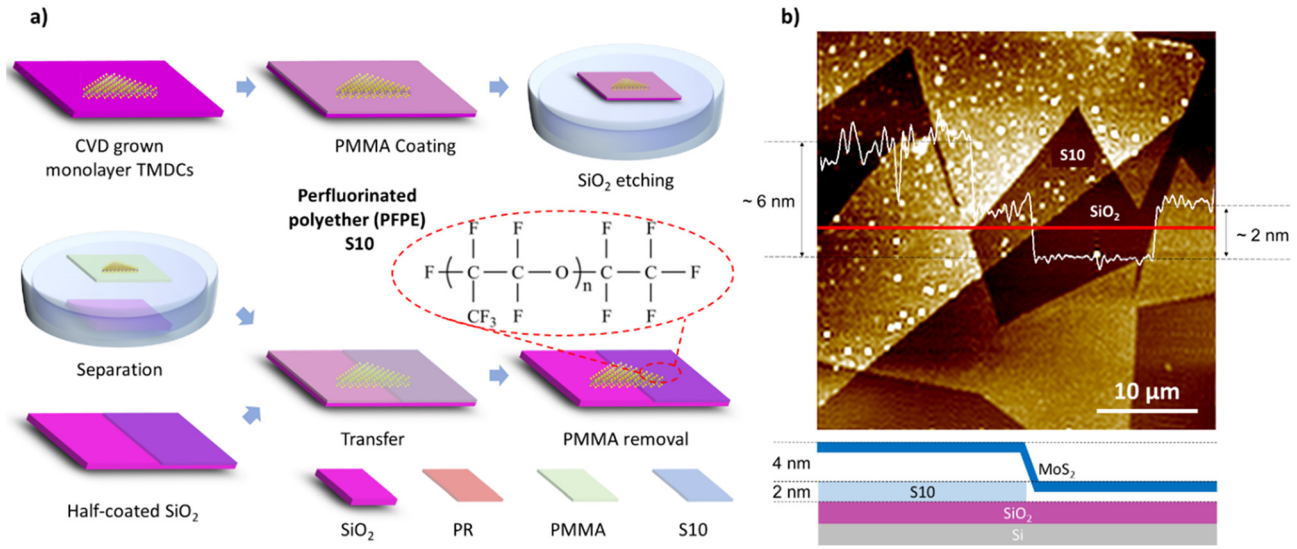

Fig. 1 Schematic of the sample preparation and the confirmation of the vdW distance: (a) wet transfer of TMDCs onto an S10 half-covered substrate and (b) AFM image of the S10/SiO_2 boundary.

in Fig. S1.† The work of the adhesion (W) at the interface is the required energy to separate the materials (peel off), and it is described below.[20]

$$W = \gamma_T + \gamma_D - \gamma_{TD} \quad (1)$$

γ_T, γ_D, and γ_{TD} are the surface energy (tension) of the TMDCs, dielectric, and the interfacial energy (interfacial surface tension) for the TMDC/dielectric interface, respectively. The conventional method to evaluate the surface energy is the contact-angle measurement. Thus, eqn (1) is typically expressed as Young's equation, as follows:

$$\gamma_{TD} = \gamma_D - \gamma_T \cos\theta \quad (2)$$

θ is the contact angle between TMDCs and the substrate, which can be 0 degrees at the flattened surface. The surface energies of MoS_2 (γ_{MoS_2}), SiO_2 (γ_{SiO_2}), and S10 (γ_{S10}) are 46.5, 115–200, and 18.14–19.86 mJ m^{-2} provide that the interfacial energies of MoS_2/SiO_2 and MoS_2/S10 are calculated as 161–246 and 64.6–66.4 mJ m^{-2}, respectively.[21,22] Thus, the increase in the vdW gap of MoS_2/S10 interfaces after S10 coating can be explained by the inverse proportion between the interfacial energy and the distance.[23] The rise of the vdW gap between MoS_2 and S10 due to the low interfacial energy (64.6–66.4 mJ m^{-2}) leads to a reduction in the coulombic interaction with the dielectric.

3.2 Optical properties of TMDCs on S10 and SiO_2

The PL property of TMDC monolayers is sensitive to the environment of TMDC/dielectric interfaces. To investigate the effect of the S10 coating, PL measurement was performed for four different TMDCs on half-covered SiO_2 by S10. The PL mapping images of four different TMDCs are shown in Fig. 2. The PL intensity of four TMDCs is dramatically improved around 4–8 times on the S10-coated area compared to the uncoated area. Interestingly, all TMDCs demonstrated that negligible changes in negative (MoS_2, $MoSe_2$, and WS_2) or positive (WSe_2) trion intensities were observed, indicating insignificant doping effects. Besides, the transition from negative or positive trion dominant features on SiO_2 to neutral exciton dominant features on S10 was confirmed by the fitting of the PL spectra of TMDCs in Fig. 2. We expected S10, the perfluorinated polyether (PFPE) polymer that can withdraw electrons from nearby molecules due to the high electronegativity of fluorine atoms, provides a strong p-type doping effect.[24,25] In contrast to our expectation, independent trion intensities according to the dielectric interface present the negligible doping effect from the substrate. According to a previous report on the heterostructure of TMDCs and perfluorinated polymer named CYTOP, the unintentional doping effect of the dielectric is prevented by CYTOP due to many body effects and band renormalization.[26] However, in the case of S10, the coulombic interaction between TMDCs and S10 is hugely suppressed by a large vdW distance of TMDCs/S10 (3.35 nm) than TMDCs/SiO_2 (1.35 nm). Therefore, the effect of surface defects of the dielectric substrate on the TMDCs is also reduced.[27] For this reason, the PL of TMDCs was improved on S10 compared to the SiO_2 substrate, as shown in Fig. 2. The two representative vibrational modes of TMDCs, denoted as A_{1g} and E^1_{2g}, are good indicators to evaluate the doping and lattice strain effect of TMDCs. In detail, the out-of-plane bending vibration A_{1g} mode has been shown to be sensitive to variations in vertical pressure and electron density due to doping.[28–30] In accordance with the surface morphology of the substrate, the in-plane bending vibration E^1_{2g} mode is shifted by strain, which is applied to the horizontal direction.[31,32] Therefore, to investigate the effect of S10, we conducted the Raman scattering

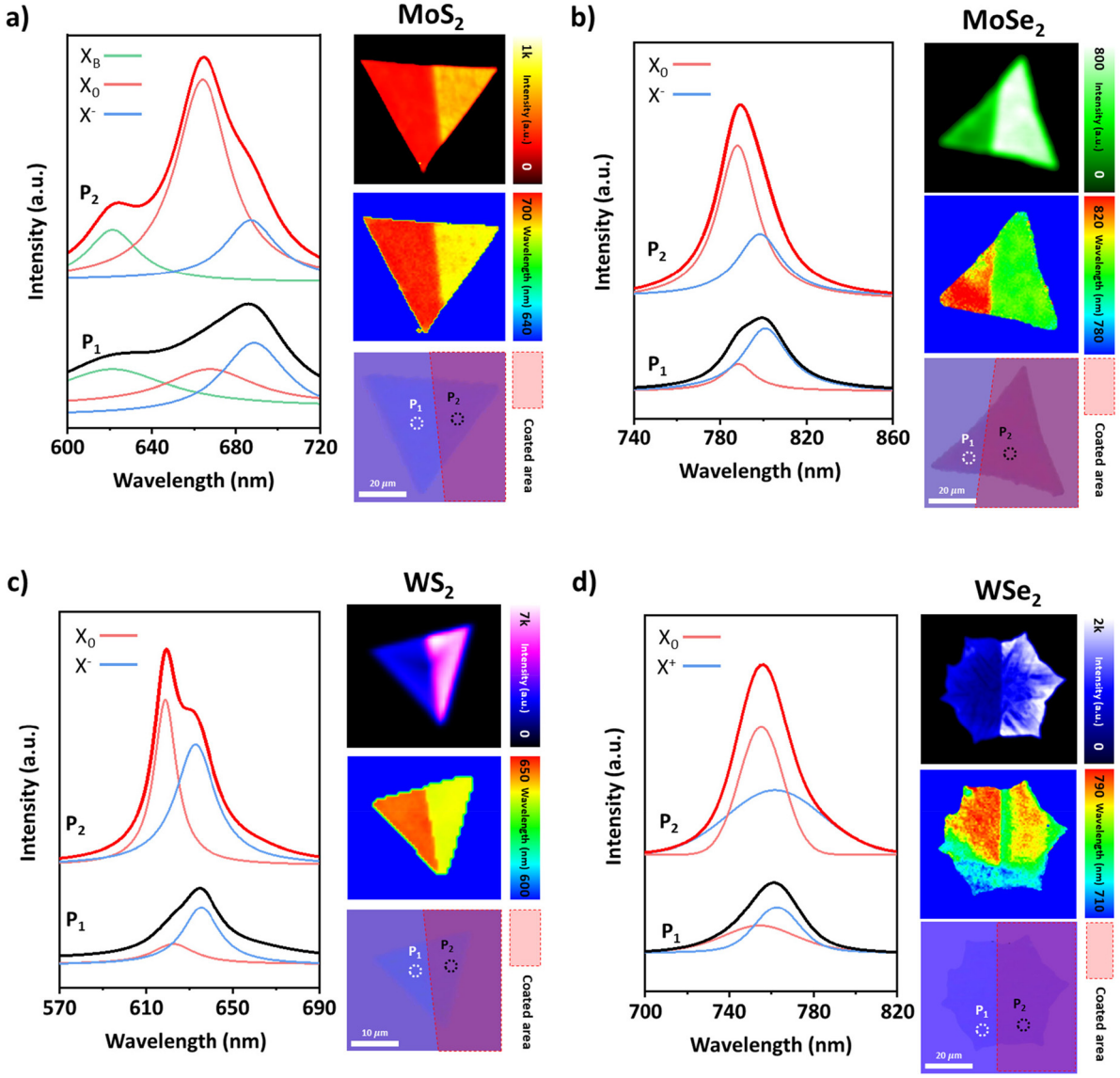

Fig. 2 PL spectra (left), mapping images (right top and middle), and optical images (right bottom) of TMDCs on the half-covered SiO_2 substrate by S10. The mapping images present the PL intensity (right top) and PL peak position at intensity maxima (right middle): (a) MoS_2, (b) $MoSe_2$, (c) WS_2, and (d) WSe_2, respectively.

measurement for TMDC monolayers, and the results are shown in Fig. 3. The Raman shift of A_{1g} and $E^1{}_{2g}$ modes shown in Fig. 3a was observed in MoS_2 with 0.4 and 0.1 cm^{-1}, respectively. However, the independent Raman modes on the substrate were confirmed from other TMDCs, as shown in Fig. 3b–d. In general, the blue shift of A_{1g} mode in MoS_2 is attributed to p-doping, which induces the conversion of negative trions to excitons in MoS_2.[28,33,34] However, the negligible change of trion in the PL spectrum of MoS_2/S10 demonstrates the insignificant p-doping effect, which leads to converting negative trions to neutral excitons. Although TMDCs generally have a significant covalent character, MoS_2 has a relatively high ionic character (4.31%), as shown in Table S1 (ESI†), and a dipole moment of 0.5 D is calculated. Therefore, despite the decrease in electrostatic interaction due to the increase in the vdW gap by the low surface energy of S10, fluorine with highest electronegativity in S10 affected the dipole moment of MoS_2, causing the shift of vibration modes.[35] Contrary to MoS_2, the peak positions of $MoSe_2$ in Fig. 3b are the same due to the relatively low ionic bonding percentage (3.73%) and dipole moment (0.45 D). The removal of unrelated peaks for the doping and strain features in Fig. 3c and d was conducted to evaluate the Raman shifts of WS_2 and WSe_2, respectively. The change seems to be negligible in WS_2 and WSe_2 as well. The negligible doping and strain relaxation are reconfirmed by the Raman shift of the A_{1g} and $E^1{}_{2g}$ modes. Therefore, a slight change in Raman scattering in MoS_2 is believed to be due to the surface morphology of the SiO_2 substrate and the widening of the vdW gap by forming PFPE SAMs with low surface energy.

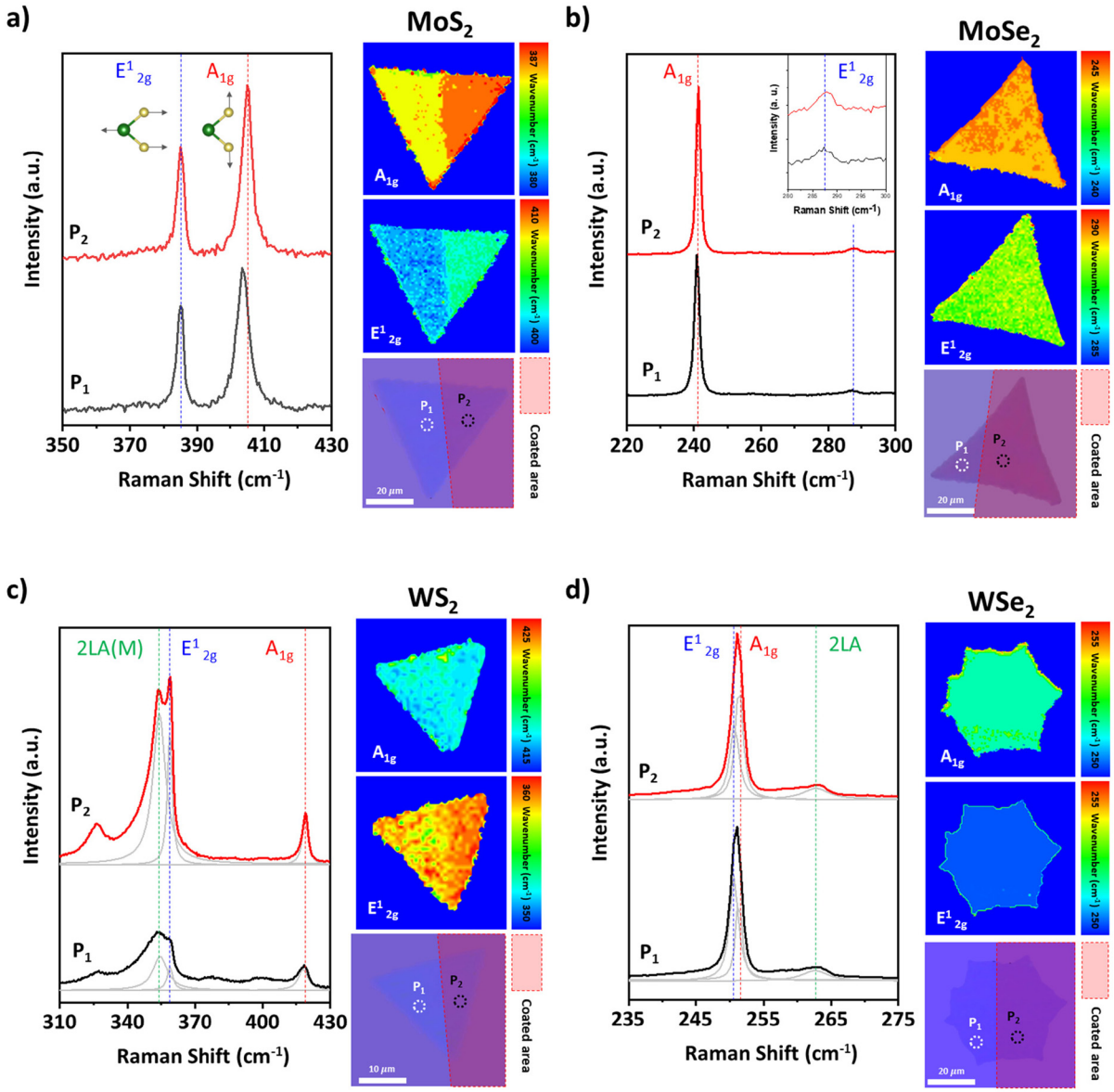

Fig. 3 Raman scattering of TMDCs on the half-covered SiO_2 substrate by S10: (a) MoS_2, (b) $MoSe_2$, (c) WS_2, and (d) WSe_2, respectively.

3.3 Binding energy of TMDCs on S10 and SiO_2

The S10 coating effect at the semiconductor/dielectric interface was analysed by PL and Raman scattering. Prior to measuring XPS for TMDs on SiO_2 and S10, we checked the formation of S10 SAM on the SiO_2 substrate, which is already observed by AFM. In Fig. S2a (ESI†), the bonding features of hydrocarbon in C 1s, the absence of a peak in F 1s, and a single peak from Si–O in the O 1s spectrum are explained for the SiO_2 substrate with some carbon impurities. However, the additional peak in the high binding energy region of C 1s, the peak rise in F 1s, and the other peaks in the O 1s spectrum clearly demonstrate the presence of the S10 layer. We then performed XPS measurements with and without S10 on the substrate to further clarify the effect of S10, and the results are shown in Fig. 4. The exact binding energies of transition metals and chalcogens in TMDCs on SiO_2 and S10 are shown in Table S2 (ESI†), and these are well matched to previous studies. Compared with SiO_2, the binding energy of TMDCs is shifted; however, the shift direction is different depending on the transition metal. Additionally, the work function changes of TMDCs on S10 as observed by ultraviolet photoelectron spectroscopy (UPS) are shown in Fig. S3,† exhibiting the same shift direction with XPS depending on transition metals. Generally, the doping effect can explain the shift of binding energy in TMDCs. However, we figure out the negligible doping effect by S10 through PL and Raman scattering. Moreover, if the doping effect of S10 is present, the direction of the binding energy shift due to it should be the same. In the case of molybdenum-based TMDCs, MoS_2 and $MoSe_2$ shown in Fig. 4a and b, the binding energy of both transition metal and

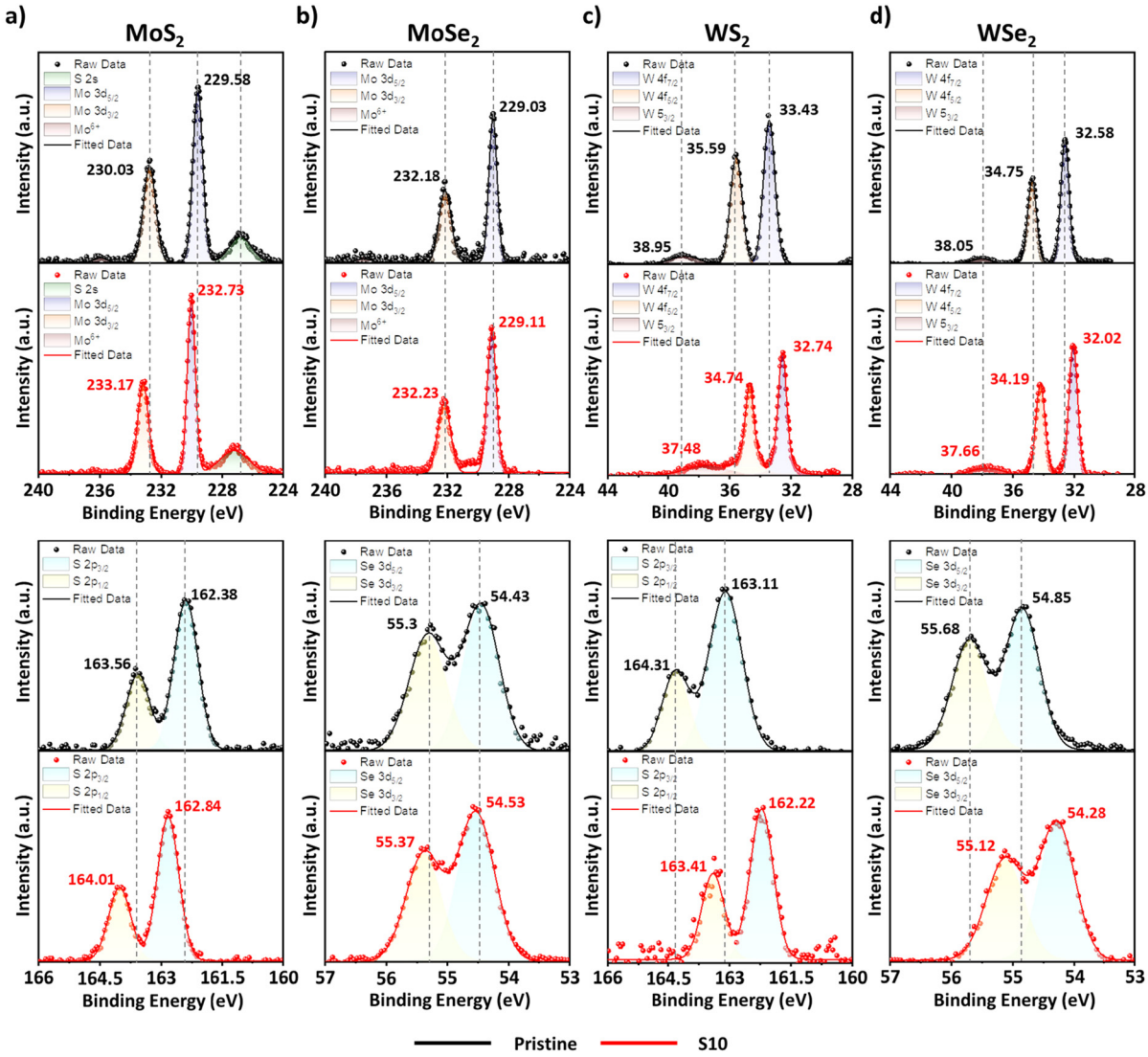

Fig. 4 Comparison of the XPS spectra of CVD-grown TMDC monolayers according to the S10 layer: (a) MoS_2, (b) $MoSe_2$, (c) WS_2, and (d) WSe_2, respectively. Black and red lines indicate SiO_2 and S10, respectively.

chalcogenide is increased on S10 and the tungsten-based TMDCs, as shown in Fig. 4c and d, are decreased. Therefore, TMDCs with different transition metals are influenced by S10 perfectly opposite. According to the previous study, the binding energy of the organic SAM layer on the Au film has been modulated in the direction of the dipole.[36] In addition, the SAM on the MoS_2 monolayer can modulate the p- or n-type doping effect by changing the orientation and magnitude of the dipole moment.[35] Generally, the permanent dipole of TMDCs is zero due to the symmetric crystal structure; however, the induced dipole moment of TMDCs by polar molecules (S10) is proportional to the electronegativity difference ($\Delta\chi$) of transition metals and chalcogens.[37] Besides, the bond character of materials can be categorized by the electronegativity differences, which are covalent bonding ($\Delta\chi < 0.4$), polar covalent bonding ($0.4 < \Delta\chi < 1.8$), and ionic bonding ($\Delta\chi > 1.8$), respectively.[24] As a result, we hypothesized that S10 affected the dipole moments of TMDCs (induced dipole), which is proved through theoretical approaches. The dipole moment can be presented using the percentage of ionic character as follows:

$$\text{Dipole moment}(\mu) = \frac{P_{\text{ionic}} eR}{100} \quad (3)$$

P_{ionic}, e, R are the percentage of ionic character, charge of the electron, and bond length, respectively. To get the ionic bonding percentage in TMDCs, we calculated using the electronegativity, as suggested by Linus Pauling, and the detailed information is shown in Table S1 (ESI†).[38]

$$\text{Ionic character } (\%) = (1 - e^{-(\Delta x/2)^2}) \times 100 \quad (4)$$

$\Delta\chi$ is the difference in electronegativity between bonded atoms, and the bond length is applied in the previous report.[39] Due to the similar electronegativity of Mo (2.16), W (2.36), S (2.58), and Se (2.55), the percentage of ionic bonding character

and the size of dipole moment are calculated as less than 5% and 0.50 D, respectively. However, those values of MoS_2 and $MoSe_2$ are larger than those of WS_2 and WSe_2 by around four times, which are more sensitive to the coulombic interaction of S10 due to the largest electronegativity of fluorine in S10. Furthermore, to confirm the effect of S10, the atomic charge densities of TMDCs with S10 were calculated by the Mulliken-dipole population analysis.[40,41] In Fig. S4 (ESI†), the atomic charge distribution of TMDCs is modulated by the S10 layer, and significant changes are observed in the charge densities of MoS_2 and $MoSe_2$ compared to those of WS_2 and WSe_2 due to the higher percentage of ionic bonding. Using the theoretical results, the dipole moment of TMDCs/S10 was calculated, and is presented in Table S3 (ESI†). The dipole moment changes in WS_2 and WSe_2 with S10 are negligible or decreased in WSe_2. In contrast, in the case of MoS_2 and $MoSe_2$, the increase in dipole moment with S10 is double. Therefore, we concluded that the opposite direction of shift in the XPS spectrum of TMDCs/S10 originated from the combined effect of charge rearrangement in TMDCs and different changes in the dipole moment by S10.

3.4 Changes in electrical properties

Experimental and theoretical approaches carefully examined the effect of S10 coating. To figure out the interface effect of S10 in electronics, a MoS_2 FET was fabricated on the half-coated S10 substrate with the bottom electrode geometry shown in Fig. 5a and b. To acquire the reproducibility of elec-

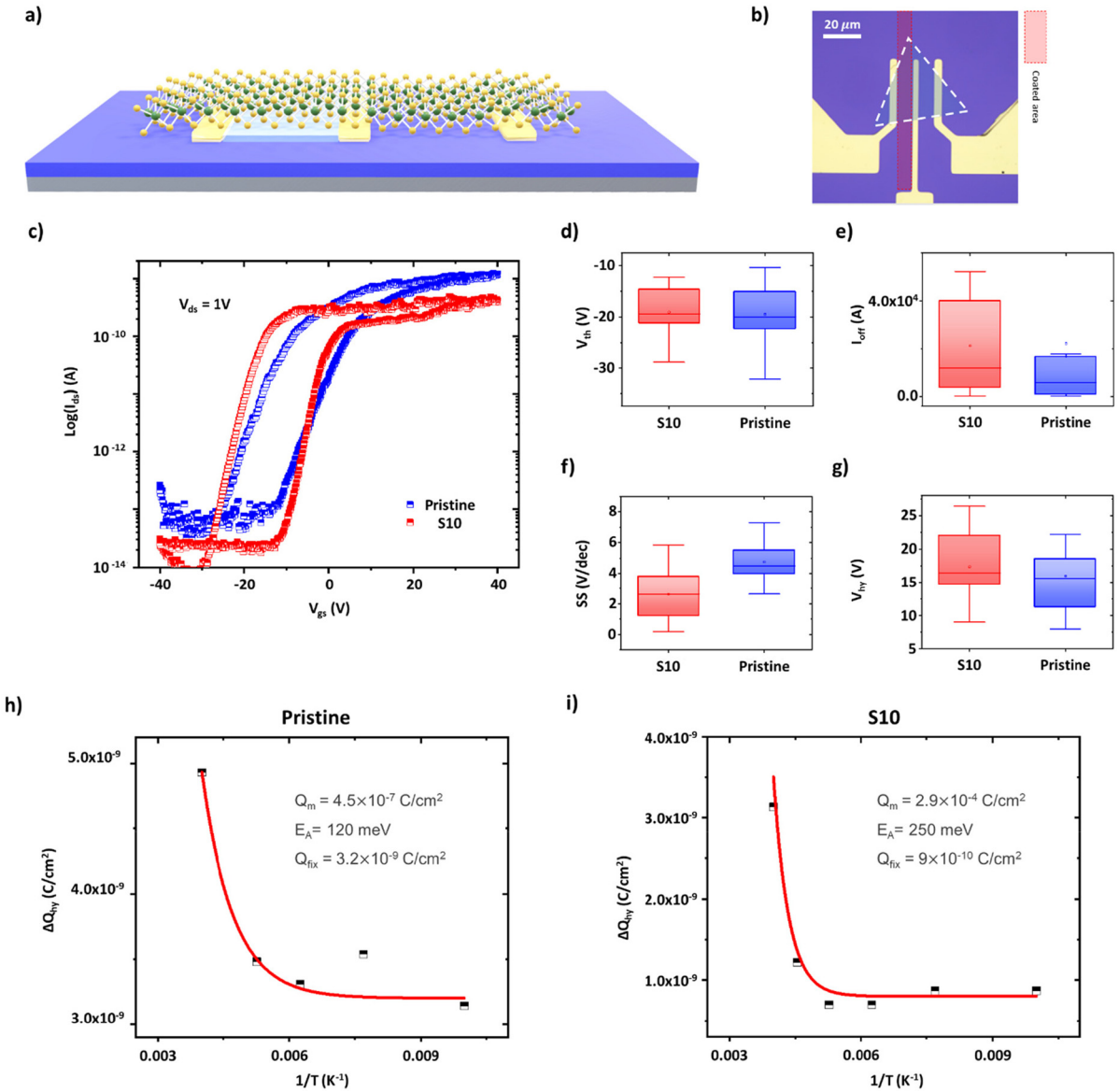

Fig. 5 Electrical properties of the CVD-grown MoS_2 monolayer depending on S10. (a) Schematic of the device and (b) optical image. (c) Representative gate sweep curve. The average electrical properties of the device for (d) threshold gate bias, (e) off current, (f) subthreshold swing value, and (g) hysteresis bias, respectively. The defect characteristics of the device with the Arrhenius approach for (h) MoS_2 on SiO_2 and (i) MoS_2 on S10.

trical properties, a total of 32 devices for each SiO_2 and S10 were fabricated, and the result is shown in Fig. S5 and S6 (ESI†), respectively. The representative transfer curves of devices are presented in Fig. 5c, and the comparisons of average electrical properties such as threshold voltage (V_{th}), off current (I_{off}), subthreshold swing (SS), and hysteresis gate bias (V_{hy}) are shown in Fig. 5d–g, respectively. According to previous studies on the perfluorinated polymer/semiconductor interface in FET, improved electrical properties with the shift of V_{th} were explained by reducing charge carrier trapping at the SiO_2 interface.[42,43] However, in this study, negligible changes except SS and field effect mobility (μ_{FE}) were observed, which indicates negligible doping effect from S10 due to the large vdW gap between MoS_2 and S10. Interestingly, the independency of SAM at the interface for the shift of V_{th} has been reported due to the low dielectric constant with extremely thin thickness.[44] Besides, the electrostatic effect of SAM acting as a dipole layer is attributed insignificantly to the change in interface for the shift of V_{th}.[45] Thus, we assume that the changes in SS values might result from the modulation of the trap state at the MoS_2/S10 interface. The trapped charge carrier in the channel at the on state can be released by thermal energy, and this process is observed as the transient current, having valuable information about the trap.[46] The transient current can be expressed using the Arrhenius equation as follows:[47]

$$\Delta Q_{hy} = Q_m \times e^{-(E_A/kT)} + Q_{fix} \quad (5)$$

$$\Delta Q_{hy} = C_{ox} \times \Delta V_T \quad (6)$$

ΔQ_{hy}, Q_m, E_A, k, T, C_{ox}, ΔV_T, and Q_{fix} are the hysteresis from eqn (6), trap charge, activation energy, Boltzmann constant, temperature, gate oxide capacitance, threshold voltage shifts, and fixed trap charge, respectively. For the analysis of the trap using the Arrhenius equation, temperature-dependent electrical measurements according to S10 were conducted, and the information of the trap was extracted from the fitted curves shown in Fig. 5h and i, respectively. Due to the changes at the interface by S10, the activation energy of interfacial defect is dramatically increased from 120 meV to 250 meV.[46] Despite the increase in mobile trap charge and activation energy, the improvement in SS values can also be understood by reducing the coulombic effect of the interfacial traps due to the large vdW gap by S10. To confirm the mitigation of substrate effects by S10 for other TMDCs, the devices were fabricated with various TMDC monolayers (MoS_2, $MoSe_2$, WS_2, and WSe_2) on the S10 layer and they exhibited modulated electrical properties compared to the conventional SiO_2 dielectric surface, as shown in Fig. S7a–d.† In particular, the introduction of PFPE SAMs increased the drain–source current (I_{DS}) of all TMDC samples, enhancing μ_{FE} by an average of about two orders of magnitude, as shown in Table S4.† Interestingly, the SS value of MoS_2 is changed noticeably from 550 mV dec^{-1} to 390 mV dec^{-1} after SAM functionalization, indicating that the coulombic interaction was weakened. The modulation of the output curves by the engineered interface is also shown in Fig. S7e and f,† which shows different I_{DS} at different back-gate biases. The pristine n-type TMDCs (MoS_2, $MoSe_2$, and WS_2) show enhanced n-type behaviours on PFPE SAMs, while the p-type WSe_2 shows enhanced p-type carrier transport. In addition, the saturation current values, which were unstable on the standard SiO_2 dielectric substrate, were stable and pronounced for each sample. Therefore, PFPE SAM has been demonstrated to enhance the electrical properties of 2D materials *via* the reduction in substrate effects with the increase in vdW distance.

4 Conclusions

In summary, we modified the vdW distance of the TMDC/dielectric interface using the low surface energy of PFPE SAM. The enhancement in PL and SS values is observed without electrical doping and strain relaxation, which is revealed by Raman scattering and electrical transport measurement. The variation in dipole moments in Mo-based TMDCs is more sensitive to W-based TMDCs with the interaction of S10 due to higher ionic bonding percentages, leading to opposite shifts of binding energy in the XPS spectra. These results provide a noble way to control the characteristics of TMDCs *via* the modulation of the vdW gap.

Author contributions

These authors contributed equally. The manuscript was written through contribution of all authors. All authors have given approval to the final version of the manuscript. Dae Young Park: conceptualization, validation, formal analysis, investigation, writing – original draft, writing – review & editing. Hyeong Chan Suh: validation, investigation, writing – original draft, visualization. Seungho Bang: writing – review & editing, formal analysis, investigation. Ju Chan Lee: investigation, formal analysis, visualization. Jaekak Yoo: methodology, investigation. Hayoung Ko: resources, validation, writing – review & editing. Soo Ho Choi: resources, validation. Ki Kang Kim: resources, validation. Seung Mi Lee: methodology, investigation, formal analysis. Tschang-Uh Nahm: formal analysis. Mun Seok Jeong: formal analysis, writing – original draft, writing – review & editing, supervision, project administration, funding acquisition.

Conflicts of interest

There are no conflicts to declare.

Acknowledgements

This work was supported by the National Research Foundation of Korea (NRF) grant funded by the Korea government (MSIT) (No. RS-2023-00260527 and 2022R1A2C2091945). This work was also supported by Material Parts Technology Development

Program ('2001710', Performance evaluation of UV Lens module mounted for semiconductor defects (less than 10 nm) inspection system) funded By the Ministry of Trade, Industry & Energy (MOTIE, Korea). D. Y. Park acknowledges support from the National Research Foundation of Korea (NRF) under grant no. NRF-2021R1I1A1A01060493. This work was partially supported (SMLee) by a National Research Council of Science & Technology (NST) grant by the Korean Government (MSIT) (no. CAP-18-04-KRISS and no. CPS23111-110).

References

1 S. Bang, N. T. Duong, J. Lee, Y. H. Cho, H. M. Oh, H. Kim, S. J. Yun, C. Park, M.-K. Kwon, J.-Y. Kim, J. Kim and M. S. Jeong, *Nano Lett.*, 2018, **18**, 2316–2323.
2 O. Lopez-Sanchez, D. Lembke, M. Kayci, A. Radenovic and A. Kis, *Nat. Nanotechnol.*, 2013, **8**, 497–501.
3 B. Radisavljevic, A. Radenovic, J. Brivio, V. Giacometti and A. Kis, *Nat. Nanotechnol.*, 2011, **6**, 147–150.
4 Y. Lee, N. Ling, D. Kim, M. Zhao, Y. A. Eshete, E. Kim, S. Cho and H. Yang, *Adv. Funct. Mater.*, 2022, **32**, 2105675.
5 K.-N. Lee, D. Y. Park, G. Choi, D. A. Nguyen, Y. C. Choi and M. S. Jeong, *ACS Appl. Mater. Interfaces*, 2020, **12**, 35716–35724.
6 K. Cho, J. Pak, S. Chung and T. Lee, *ACS Nano*, 2019, **13**, 9713–9734.
7 B.-K. Kim, T.-H. Kim, D.-H. Choi, H. Kim, K. Watanabe, T. Taniguchi, H. Rho, J.-J. Kim, Y.-H. Kim and M.-H. Bae, *npj 2D Mater. Appl.*, 2021, **5**, 1–10.
8 L. Liu, L. Kong, Q. Li, C. He, L. Ren, Q. Tao, X. Yang, J. Lin, B. Zhao, Z. Li, Y. Chen, W. Li, W. Song, Z. Lu, G. Li, S. Li, X. Duan, A. Pan, L. Liao and Y. Liu, *Nat. Electron.*, 2021, **4**, 342–347.
9 X. Fan, R. Nouchi and K. Tanigaki, *J. Phys. Chem. C*, 2011, **115**, 12960–12964.
10 Y. Zhang, V. W. Brar, C. Girit, A. Zettl and M. F. Crommie, *Nat. Phys.*, 2009, **5**, 722–726.
11 H. Jeong, H. M. Oh, A. Gokarna, H. Kim and S. J. Yun, *Adv. Mater.*, 2017, **29**, 1700308.
12 H. Chen, J. Li, X. Chen, D. Zhang and P. Zhou, *Semicond. Sci. Technol.*, 2018, **33**, 024001.
13 J. Wierzbowski, J. Klein, F. Sigger, C. Straubinger, M. Kremser, T. Taniguchi, K. Watanabe, U. Wurstbauer, A. W. Holleitner, M. Kaniber, K. Müller and J. J. Finley, *Sci. Rep.*, 2017, **7**, 1–6.
14 D. Liu, X. Chen, Y. Yan, Z. Zhang, Z. Jin, K. Yi, C. Zhang, Y. Zheng, Y. Wang, J. Yang, X. Xu, J. Chen, Y. Lu, D. Wei, A. T. S. Wee and D. Wei, *Nat. Commun.*, 2019, **10**, 1–11.
15 C. Lee, S. Rathi, M. A. Khan, D. Lim, Y. Kim, S. J. Yun, D.-H. Youn, K. Watanabe, T. Taniguchi and G.-H. Kim, *Nanotechnology*, 2018, **29**, 335202.
16 D. G. Purdie, N. M. Pugno, T. Taniguchi, K. Watanabe, A. C. Ferrari and A. Lombardo, *Nat. Commun.*, 2018, **9**, 5387.
17 P. V. Pham, S. C. Bodepudi, K. Shehzad, Y. Liu, Y. Xu, B. Yu and X. Duan, *Chem. Rev.*, 2022, **122**, 6514–6613.
18 J. S. Lee, S. H. Choi, S. J. Yun, Y. I. Kim, S. Boandoh, J.-H. Park, B. G. Shin, H. Ko, S. H. Lee, Y.-M. Kim, Y. H. Lee, K. K. Kim and S. M. Kim, *Science*, 2018, **362**, 817–821.
19 H. Ko, S. H. Choi, J. Kim, Y. I. Kim, Y.-H. Kim, L. A. Adofo, M.-H. Jung, Y.-M. Kim, M. S. Jeong, K. K. Kim and S. M. Kim, *2D Mater.*, 2021, **8**, 034003.
20 A. A. Volinsky, N. R. Moody and W. W. Gerberich, *Acta Mater.*, 2002, **50**, 441–466.
21 S. Deng, E. Gao, Z. Xu and V. Berry, *ACS Appl. Mater. Interfaces*, 2017, **9**, 7812–7818.
22 J. Huo, J. Xiao, T. V. Kirk and X. D. Chen, *Food Bioprod. Process.*, 2019, **118**, 130–138.
23 M. Wang, G. Zhang, H. Xu and Y. Fu, *Materials*, 2020, **13**, 1681.
24 D. D. Ebbing, S. D. Gammon and R. O. Ragsdale, *Essentials of General Chemistry*, Houghton Mifflin, 2006.
25 V. Z. Poenitzsch, D. C. Winters, H. Xie, G. R. Dieckmann, A. B. Dalton and I. H. Musselman, *J. Am. Chem. Soc.*, 2007, **129**, 14724–14732.
26 B. Liu, W. Zhao, Z. Ding, I. Verzhbitskiy, L. Li, J. Lu, J. Chen, G. Eda and K. P. Loh, *Adv. Mater.*, 2016, **28**, 6457–6464.
27 D. Wang and R. Sundararaman, *Phys. Rev. Mater.*, 2019, **3**, 083803.
28 Z. Wang, M. Tripathi, Z. Golsanamlou, P. Kumari, G. Lovarelli, F. Mazziotti, D. Logoteta, G. Fiori, L. Sementa, G. M. Marega, H. G. Ji, Y. Zhao, A. Radenovic, G. Iannaccone, A. Fortunelli and A. Kis, *Adv. Mater.*, 2023, **35**, e2209371.
29 M. M. Petrić, M. Kremser, M. Barbone, Y. Qin, Y. Sayyad, Y. Shen, S. Tongay, J. J. Finley, A. R. Botello-Méndez and K. Müller, *Phys. Rev. B*, 2021, **103**, 035414.
30 T. Lee, K.-Y. Lee, Y.-J. Lee, C.-H. Cho and H. Rho, *Curr. Appl. Phys.*, 2023, **49**, 115–119.
31 S. H. Choi, H.-J. Kim, B. Song, Y. I. Kim, G. Han, H. T. T. Nguyen, H. Ko, S. Boandoh, J. H. Choi, C. S. Oh, H. J. Cho, J. W. Jin, Y. S. Won, B. H. Lee, S. J. Yun, B. G. Shin, H. Y. Jeong, Y.-M. Kim, Y.-K. Han, Y. H. Lee, S. M. Kim and K. K. Kim, *Adv. Mater.*, 2021, **33**, e2006601.
32 J. T. Mlack, P. Masih Das, G. Danda, Y.-C. Chou, C. H. Naylor, Z. Lin, N. P. López, T. Zhang, M. Terrones, A. T. C. Johnson and M. Drndić, *Sci. Rep.*, 2017, **7**, 43037.
33 S. Mouri, Y. Miyauchi and K. Matsuda, *Nano Lett.*, 2013, **13**, 5944–5948.
34 M. Li, J. Yao, X. Wu, S. Zhang, B. Xing, X. Niu, X. Yan, Y. Yu, Y. Liu and Y. Wang, *ACS Appl. Mater. Interfaces*, 2020, **12**, 6276–6282.
35 Y. Wang, S. M. Gali, A. Slassi, D. Beljonne and P. Samorì, *Adv. Funct. Mater.*, 2020, **30**, 2002846.
36 T. C. Taucher, I. Hehn, O. T. Hofmann, M. Zharnikov and E. Zojer, *J. Phys. Chem. C*, 2016, **120**, 3428–3437.
37 C. P. Smyth, *J. Phys. Chem.*, 1937, **41**, 209–219.
38 L. Pauling, *J. Am. Chem. Soc.*, 1932, **54**, 3570–3582.

39 M. Velický and P. S. Toth, *Appl. Mater. Today*, 2017, **8**, 68–103.
40 D. Voß, P. Krüger, A. Mazur and J. Pollmann, *Phys. Rev. B*, 1999, **60**, 14311–14317.
41 J. P. Perdew, K. Burke and M. Ernzerhof, *Phys. Rev. Lett.*, 1996, **77**, 3865–3868.
42 Y. Yang, Y. Hong and X. Wang, *ACS Appl. Mater. Interfaces*, 2021, **13**, 8682–8691.
43 P. J. Diemer, Z. A. Lamport, Y. Mei, J. W. Ward, K. P. Goetz, W. Li, M. M. Payne, M. Guthold, J. E. Anthony and O. D. Jurchescu, *Appl. Phys. Lett.*, 2015, **107**, 103303.
44 M. Aghamohammadi, R. Rödel, U. Zschieschang, C. Ocal, H. Boschker, R. T. Weitz, E. Barrena and H. Klauk, *ACS Appl. Mater. Interfaces*, 2015, **7**, 22775–22785.
45 S. K. Possanner, K. Zojer, P. Pacher, E. Zojer and F. Schürrer, *Adv. Funct. Mater.*, 2009, **19**, 958–967.
46 J. Lee, M. J. Kim, B. G. Jeong, C. Kwon, Y. Cha, S. H. Choi, K. K. Kim and M. S. Jeong, *Appl. Surf. Sci.*, 2023, **613**, 155900.
47 Y. Park, H. W. Baac, J. Heo and G. Yoo, *Appl. Phys. Lett.*, 2016, **108**, 083102.